Phys Chem Minerals (2006) 33: 276–287
DOI 10.1007/s00269-006-0079-9

ORIGINAL PAPER

Monika Koch-Müller · Stanislav S. Matsyuk
Dieter Rhede · Richard Wirth · Natasha Khisina

Hydroxyl in mantle olivine xenocrysts from the Udachnaya kimberlite pipe

Received: 10 October 2005 / Accepted: 23 February 2006 / Published online: 4 April 2006

Abstract The incorporation of hydrogen in mantle olivine xenocrysts from the Udachnaya kimberlite pipe was investigated by Fourier-transform infrared spectroscopy and secondary ion mass spectrometry (SIMS). IR spectra were collected in the OH stretching region on oriented single crystals using a conventional IR source at ambient conditions and in situ at temperatures down to −180°C as well as with IR synchrotron radiation. The IR spectra of the samples are complex containing more than 20 strongly polarized OH bands in the range 3,730–3,330 cm^{-1}. Bands at high energies (3,730–3,670 cm^{-1}) were assigned to inclusions of serpentine, talc and the 10 Å phase. All other bands are believed to be intrinsic to olivine. The corresponding point defects are (a) associated with vacant Si sites (3,607 cm^{-1} $E \parallel a$, 3,597 $E \parallel a$, 3,571 cm^{-1} $E \parallel c$, 3,567 $E \parallel c$, and 3,556 $E \parallel b$), and (b) with vacant M1 sites (most of the bands polarized parallel to *a*). From the pleochroic behavior and position of the OH bands associated with the vacant M1 sites, we propose two types of hydrogen—one bonded to O1 and another to O2, so that both OH vectors are strongly aligned parallel to *a*. The O2–H groups may be responsible for the OH bands at higher wavenumbers than those for the O1–H groups. The multiplicity of the corresponding OH bands in the spectra can be explained by different chemical environments and by slightly different distortions of the M1 sites in these high-pressure olivines. Four samples were investigated by SIMS. The calculated integral molar absorption coefficient using the IR and SIMS results of 37,500 ± 5,000 L mol H_2O cm^{-2} is within the uncertainties slightly higher than the value determined by Bell et al. (J Geophys Res 108(B2):2105–2113, 2003) (28,450 ± 1,830 L mol H_2O cm^{-2}). The reason for the difference is the different distributions of the absorption intensity of the spectra of both studies (mean wavenumber 3,548 vs. 3,570 cm^{-1}). Olivine samples with a mean wavenumber of about 3,548 cm^{-1} should be quantified with the absorption coefficient as determined in this study; those containing more bands at higher wavenumber (mean wavenumber 3,570 cm^{-1}) should be quantified using the value determined by Bell et al. (J Geophys Res 108(B2):2105–2113, 2003).

Keywords OH^- in olivine · IR spectroscopy · Synchrotron IR · SIMS · Point defects

Introduction

Hydrogen incorporation in olivine has been the object of numerous studies (e.g., Beran 1969; Beran and Putnis 1983; Kitamura et al. 1987; Miller et al. 1987; Bai and Kohlstedt 1993; Libowitzky and Beran 1995; Kohlstedt et al. 1996; Kurosawa et al. 1997; Khisina et al. 2001; Lemaire et al. 2004; Bell et al. 2003; Matsyuk and Langer 2004; Zhao et al. 2004). It is clear that olivine contains traces of hydrogen chemically bound as hydroxyl and incorporated not only as intrinsic but also as extrinsic defects. Most of the studies focused on infrared spectroscopic characterization and quantification of the hydroxyl groups in olivine. However, despite all these efforts, the olivine IR spectra in the OH stretching region and thus the incorporation mechanisms are still incompletely understood (Matsyuk and Langer 2004). One reason for that is the wide variability and com-

M. Koch-Müller (✉) · D. Rhede · R. Wirth
GeoForschungsZentrum Potsdam, Department 4, Telegrafenberg, 14473 Potsdam, Germany
E-mail: mkoch@gfz-potsdam.de
Tel.: +49-331-2881492

S. S. Matsyuk
Institute of Geochemistry, Mineralogy and Ore Formation, National Academy of Sciences of Ukraine, Palladin Ave., 34, 03680 Kyiv, Ukraine

N. Khisina
V.I.Vernadsky Institute of Geochemistry and Analytical Chemistry of Russian Academy of Science, Kosigin St., 19, 119991 GSP-1, 334 Moscow, Russia

plexity of the spectra, especially of natural mantle olivine (e.g., Miller et al. 1987; Matsyuk and Langer 2004). Generally, kimberlitic olivine shows the highest water[1] content (about 400 ppm by wt) whereas those from basaltic flows, such as San Carlos olivine are very dry (1–3 ppm by wt) (Miller et al. 1987; Bai and Kohlstedt 1993). Matsyuk and Langer (2004) investigated 174 different specimens of the Yakutian upper mantle and described up to 70 different OH bands: 17 are assigned to nonintrinsic separate inclusions but 52 to defects, intrinsic to olivines. Olivine from different geological settings incorporates hydrogen in different ways and quantities. Experimental studies confirm that the incorporation of hydrogen in olivine depends strongly on the chemical environment, especially the silica activity, and increases with increasing water fugacity, oxygen fugacity, pressure, temperature and Fe content (e.g., Bai and Kohlstedt 1993; Kohlstedt et al. 1996; Matveev et al. 2001; Lemaire et al. 2004; Zhao et al. 2004).

Intrinsic OH defects in olivine are suggested to occur by substitution of O^{2-} by OH^- either charge balanced by cation vacancies at the M sites $(2H)^x_{Mg}$ (e.g., Bai and Kohlstedt 1993; Kohlstedt et al. 1996; Zhao et al. 2004) and/or at the silicon sites $(4\,H)^x_{Si}$ (e.g., Libowitzky and Beran 1995; Matveev et al. 2001; Braithwaite et al.2003; Lemaire et al. 2004). Incorporation of hydrogen through coupled substitution like $B^{3+} + H^+ = Si^{4+}$ has been described (Sykes et al. 1994) but seems to be very limited. However, olivine is also known as host for hydrous minerals incorporated as micrometer- to nanometer-sized inclusions, which contribute to the complex OH absorption spectra. The most common inclusions contain the minerals serpentine, talc and Ti-clinohumite (e.g., Kitamura et al. 1987; Miller et al. 1987; Khisina et al. 2001; Matsyuk and Langer 2004). More rare inclusions of Mg-edenite, Mg-pargasite, hydrous wadsleyite and the 10 Å phase have been observed (Khisina et al. 2001; Matsyuk and Langer 2004). Khisina et al. (2001) report on nanometer-sized inclusions of hydrous olivine from a mantle xenolith from the Udachnaya pipe.

In the last 5 years, several studies focused on OH in olivine using experimental and theoretical approaches to improve the band assignment for the OH bands in the olivine spectra, and thus help to understand the OH incorporation mechanisms (e.g., Matveev et al. 2001; Braithwaite et al. 2002, 2003; Lemaire et al. 2004; Zhao et al. 2004; Matveev et al. 2005). Our approach is to apply these results to the complex mantle olivine from kimberlites. Therefore, we selected a series of samples from the Udachnaya kimberlite pipe. We found both defects, the one associated with a vacant Si site and another associated with a vacant M site occur in the kimberlitic olivines. The latter defect more pronounced and we propose that it is associated with vacancies at the M1 site. However, OH associated with this defect is in these high-pressure olivines incorporated in a quite different way than described for synthetic olivine.

Experimental

Sample description

We have chosen nine xenocryst samples from the Udachnaya kimberlite pipe for our investigation (Table 1). From the optical appearance, we can subdivide the samples into two series: olivines from series A (Ud-170, Ud-114, Ud-52, Udf-43, F-43 and F-64) show more or less pronounced optically visible microstructure (OVM) formed by cross-hatched linear features and olivines from series B (Ud-29, Ud-85, F-69) were optically clear (OC). TEM investigations showed that the OVM corresponds to water-bearing nano-inclusions of hydrous olivine, 10 Å phase, serpentine and talc (R. Wirth et al., submitted).

Secondary ion mass spectrometry

The trace element contents of four olivine samples were analyzed by secondary ion mass spectrometry (SIMS) using the CAMECA ims 6f ion probe at the GFZ Potsdam. A 100 nA mass-filtered primary $^{16}O^-$ beam was accelerated to 12.5 kV and focused to form a ~60–80 µm diameter beam on the sample surface. An 8-min presputtering was applied to reduce surface contamination. The secondary accelerating potential was 10 kV and the energy slit was set to a width corresponding to 25 V. Energy filtering was applied to suppress molecular interferences (−100 V offset) and measured $^1H^+$, $^7Li^+$, $^{11}B^+$, $^{27}Al^+$, $^{30}Si^+$, $^{40}Ca^+$, $^{52}Cr^+$ and $^{55}Mn^+$ intensities was normalized to $^{30}Si^+$. Counting times per cycle were 10 s for ^1H, ^7Li, ^{11}B, 2 s for ^{30}Si and 5 s for the other isotopes. The mass resolution was $(M/\Delta M)$ 300 and entrance and exit slit were fully open. All samples were mounted on SiO_2 glass disks using the minimum possible amount of epoxy resin. The sample disks were cleaned individually in an ultrasonic bath using high-purity ethanol, were stored at 70°C under low vacuum, were coated with ~30 nm high-purity gold and were put into the airlock chamber to outgas at a pressure better than 3×10^{-7} Pa for more than 3 days. The multielement reference NBS-glasses 610, 612 and 614 were used for the construction of calibration curves of all isotopes but $^1H^+$. For $^1H^+$ measurements relative sensitivity factors were determined from multiple analyses of seven gem quality garnet reference samples whose H_2O contents had been established independently using other techniques and which range between 17 and 870 ppm (Maldener et al. 2003).

The results of the first hydrogen measurements have shown the necessity to improve the analytical conditions. At first, prior to each analytical session, the entire

---

[1] It is a common sense to express the hydroxyl concentration in terms of ppm by wt water

Table 1 Olivine xenocrysts from Udachnaya kimberlite pipe (Yakutia)

Sample no.	Association	Prepared crystals Orientation	Characteristics			Fay (%)	$A_{i,\mathrm{tot}}$ (mm^{-1})	H_2O ppm by wt IR (Bell et al. 2003)	H_2O ppm by wt IR (this study)
			t (mm)	Color	Microstructure and inclusions				
Ud-29[a]	Ol-xenocryst with included Sp[b]	(100) (010)	1.31 1.21	Yellow green (010)	Optically clear	7.1	108	207	156
Udf-43	Ol-xenocryst with included Gt[b]	(010) (001)	0.592 0.658	Light–light yellow green (010)	Linear features visible in (010) and (001)	7.3	61	116	89
Ud-85[a]	Ol-xenocryst	(010) (001)	2.912 1.283	Light–light yellow green (010)	Optically clear	7.8	25	49	37
F-43[a]	Ol-xenocryst	(100) (001)	0.536 0.458	Light yellow green (100)	Very weak linear features	7.8	164	314	237
Ud-170[a]	Ol-xenocryst with included Cpx	(010) (100)	0.801 0.947	Light yellow green (100)	Linear features visible in (010) and (100)	7.9	167	320	244
Ud-114[a]	Ol-xenocryst	(010) (001)	1.37 0.952	Olive green (010)	Linear features visible in (010) and (001)	8.2	153	293	224
F-64[a]	Ol-xenocryst	(100) (001)	0.463 0.732	Light yellow green (100)	Very weak linear features	8.0	84	161	123
Ud-52	Ol-xenocryst with Ilm-lamellae	(010) (001)	0.812 0.56	Light olive (001)	Linear features visible in (010) and (001)	11.9	156	298	228
F-69[a]	Ol-xenocryst	(010) (001)	0.778 0.652	Light brown (010)	Optically clear	15.0	205	392	300

For abbreviations of mineral phases: *Gt* garnet, *Ol* olivine, *Cpx* clinopyroxene, *Sp* spinel, *Ilm* ilmenite, *D* diamond, *Py* pyrope

[a] Prepared as parallelepipeds

[b] Sp: $Cr_2O_3 = 64.73$, $Al_2O_3 = 5.55$ (D-Py-Fazies), Gt: $Cr_2O_3 = 11.02$, $CaO = 4.76\%$ (D-Py-Fazies)

instrument was baked for at least 48 h. Furthermore, improvements to the vacuum system (Wiedenbeck et al. 2004) and a permanently filled liquid nitrogen Dewar guaranteed that the total vacuum pressure in the sample chamber during the measurements was always $<4.0\times10^{-8}$ Pa. The $^{16}O^-$ primary beam analytical setup employed a 12.5 kV, 50 nA beam focused to a 20–30 µm diameter spot on the sample surface. The primary ion beam was scanned over an 80 µm×80 µm area. Positive secondary ions were extracted using a 10 kV potential and were subsequently energy filtered by applying a −150 V offset to sample in conjunction with an energy slit which was adjusted to a width corresponding to 100 V. Fully open entrance and exit slits were used in combination with a 60 µm field-of-view as defined by the instrument's transfer optics and a 750 µm field aperture. Furthermore, an electronic gate equivalent to a 20 µm×20 µm area and centered on the middle of the raster guaranteed that only those ions emitted from the center of the sputter crater were collected. The scanning ion imaging capability of the Cameca 6f was then used to verify the absence of any crater wall effects. Counting times per cycle were 10 s for ^1H and 2 s for ^{30}Si. The duration of sputtering required to achieve steady-state conditions (i.e., $^1H^+/^{30}Si^+$ ratio becoming constant) varied as a function of the H_2O concentration and hence the total time of data acquisition often need to be extended to over 120 min for the most H-depleted samples. The $^1H^+/^{30}Si^+$ ratios used to establish the working curve were calculated by averaging only the final 50 cycles from each analysis.

Repeated, independent analytical sessions using an $^{16}O^-$ primary beam demonstrate the critical importance of recalibrating the relative ion yields, as the slope of the calibration line was found to change by as much as 13% between session despite using identical instrument settings and having similar vacuum conditions (D. Rhede and M. Wiedenbeck, submitted).

IR spectroscopy

We collected polarized single-crystal IR spectra in the range of 2,500–4,000 cm^{-1} of all nine samples using a Bruker ISF 66v spectrometer attached with a Hyperion microscope. The spectra were collected with the electrical vector of the polarized radiation *E* parallel to the optical indicatrix axes ($E \parallel n_\gamma \parallel a$; $E \parallel n_\alpha \parallel b$ and $E \parallel n_\beta \parallel c$). The spectra were taken with an aperture of 80 µm×80 µm in OC parts of the crystals at ambient conditions. Some spectra were collected at −180°C using a Linkam FTIR600 heating/freezing stage. We also collected polarized spectra using synchrotron IR radiation at the IR beamline at Bessy II with a local resolution down to 5 µm×5 µm.

To quantify the hydrogen content, we calculated the total absorbances of the OH bands by summing the integral absorbances along the indicatrix axis $A_{i,\mathrm{tot}} = A_{n\alpha} + A_{n\beta} + A_{n\gamma}$ and used the recent calibration of Bell et al. (2003) and the calibration obtained in this study.

To probe the hydrogen incorporation mechanism, we dehydrated one sample (Ud-170) through stepwise heating (from 450°C in 50°C steps) the sample in air up to 950°C. At each temperature, the sample was hold for 24 h in air and quenched to investigate them by Fourier-transform infrared (FTIR) spectroscopy. For comparison, one sample (Ud-52) was annealed under controlled oxygen fugacity of $10^{-18.5}$ at 800°C (close to the magnetite/wüstite buffer) for 24 h in a vertical rapid-quench furnace. The oxygen fugacity was controlled by a mixture of CO_2 and H_2 gas that flowed past the specimen. Oxygen fugacity was monitored using a zirconia-based solid electrolyte oxide sensor with air as reference gas.

Results

The spectra of all nine samples show OH stretching bands in the range of 3,730–3,330 cm^{-1} but with different intensities (Fig. 1). The spectra are characterized by a high absorption with $E \parallel a \parallel (n_\gamma)$ (about 80% of $A_{i,\mathrm{tot}}$) and less with $E \parallel b \parallel (n_\alpha)$ and $E \parallel c \parallel (n_\beta)$ (Fig. 2). Based on the calibration of Bell et al. (2003), the hydrogen content (expressed as ppm by wt H_2O) ranges from 49 to 392 wt ppm H_2O and with the calibration obtained in this study from 37 to 300 wt ppm H_2O (Table 1). All samples—those with and those without microstructure—do contain OH bands in the region 3,730–3,670 cm^{-1} which we assigned to the inclusions of serpentine, talc and 10 Å phase.

In the region from 3,650 to 3,330 cm^{-1}, we observe at least 20 OH bands (Fig. 1 and Table 2). Most of the bands can be observed in all nine samples but with different intensities. There is no direct correlation between the water content and the observed microstructure (Table 1). Also, there is no correlation between the pattern of the IR spectra and the observed microstructure: the infrared spectra of samples Ud-114 (OVM) and F-43 (OC) are nearly identical (Fig. 1, Table 1; and Fig. 3 in R. Wirth et al., submitted). Therefore, we assign all these OH bands to hydroxyl groups intrinsic to the olivine lattice as point defects although a small contribution must come from stretching vibrations of hydroxyl groups in hydrous olivine (Hy-2a) which has been observed by TEM in some of the samples. However, we estimate its contribution to the IR spectra to be small and may be hidden in the complex structures of the spectra.

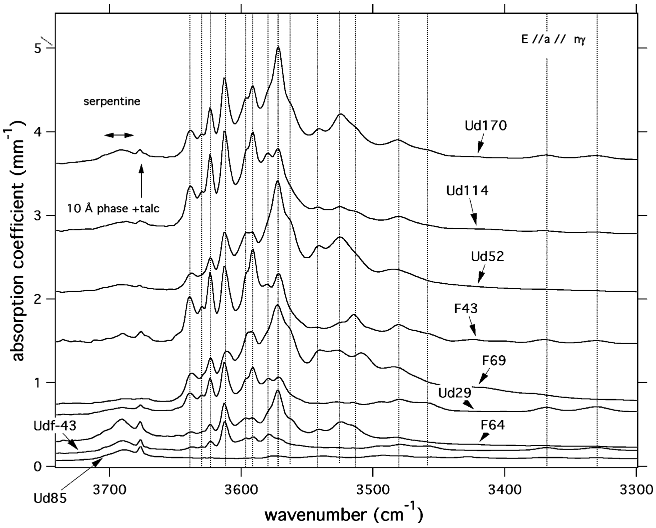

Fig. 1 Polarized infrared spectra of olivine with $E \parallel a$ ($n\gamma$). The spectra are normalized to a thickness of 1 mm and offset for clarity

Pleochroism and spectra taken at −180°C

The OH bands are strongly pleochroic (Fig. 2). We can distinguish four types of OH bands based on their polarization behavior (Table 2). At least 12 of the 20 OH bands (nearly all the bands between 3,650 and 3,580 cm^{-1}) show the highest absorption with $E \parallel a$ and nearly no or only small absorption with $E \parallel b$ and/or $E \parallel c$ ($a >>> b, c$). We call this as type-I bands. Type-II bands show high absorption with E parallel to a, but there is also absorption with $E \parallel b$ and with $E \parallel c$ ($a >> c > b$). Type-III bands show a strong absorption with E parallel to c ($c >> a$ and b). Type-IV bands show a strong absorption with $E \parallel b$ and c, less with $E \parallel a$ ($b > c > a$). It is hard to distinguish the different types in the complex spectra due to band overlapping. Figure 3 compares the IR spectra of sample Ud−114 taken at ambient conditions with those taken at −180°C. With decreasing temperature, the OH bands shift to higher energies and overlapping bands get separated. In the spectral region around 3,610–3,615 cm^{-1}, it becomes clear that the one band observed at ambient condition consists of at least three type-I bands with strong absorption with $E \parallel a$. The spectral region around 3,567–3,573 cm^{-1} is also a very complex indication that the strong band at 3,572 cm^{-1} at room temperature with type-II polarization has contributions of at least two bands with type-III polarization. Figure 4 compares the spectra of Ud-114 and Ud-52 both taken at −180°C. At least one OH band of type-I, three OH bands of type-III and one OH band of type-IV (arrows in Fig. 4) can be observed in the low temperature spectra of the sample Ud-114 and which are absent or very weak in the spectra of the sample Ud-52. A careful analysis of the spectra of all samples reveals that the additional (or much more intensive) bands described above also occur or are much more pronounced in samples F-43, Ud-29 and Udf-43. Interestingly, these bands (3,607 cm^{-1} $E \parallel a$, 3,571 cm^{-1} $E \parallel c$, 3,567 $E \parallel c$, 3,556 $E \parallel b$) coincide with band position and polarization behavior with OH bands of synthetic olivine assigned by Lemaire et al. (2004) to OH point defects in association with vacant silicon sites.

Band correlation analyses

To assign the OH bands to different point defects, band correlation analysis is very useful. Only the linear absorbances (A_{lin}) of the most intense bands were analyzed. We found two groups of correlations. Correlation

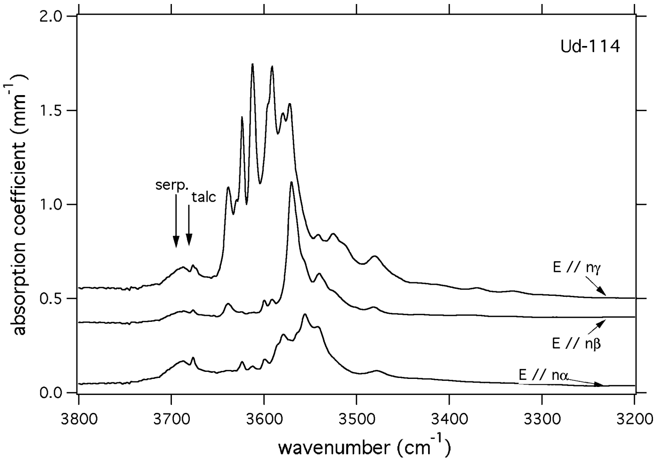

Fig. 2 Polarized infrared spectra of olivine sample Ud-114

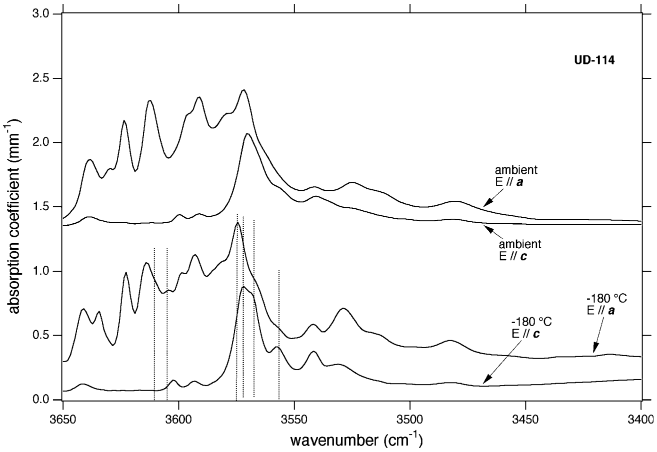

Fig. 3 Polarized infrared spectra of olivine sample Ud-114 taken at room temperature and in situ at −180°C

group I is characterized by positive correlations ($r^2 = 0.870$–0.929) of A_{lin} of the OH bands at 3,612–3,613 ($E \parallel a$), 3,567–3,571 ($E \parallel c$), 3,555–3,556 ($E \parallel b$) and 3,580 ($E \parallel a$) cm^{-1} assigned by Lemaire et al. (2004) as OH point defects in association with vacant silicon sites. All the other bands, i.e., 3,639, 3,630, 3,624, 3,612–3,613, 3,597, 3,591 and 3,580 cm^{-1} which are all polarized parallel to *a* also show positive correlations ($r^2 = 0.745$–0.966) between their linear absorbances. The band system around 3,612–3,613 and 3,580 cm^{-1} appears in group I and group II correlations which is due to the above-mentioned band overlap.

Table 2 OH-bands intrinsic to olivine UD-114

Band no. after Matsyuk and Langer (2004)	ν (cm^{-1})		OH-band type[a]	Remarks
	Ambient	−180°C		
10	3,639	3,640	I	
11	3,630	3,634	I	
12	3,624	3,623	I	
14	3,612	3,614	I	
15⇒		3,607	I	Strong in Ud-114, Ud-29, Udf-43, F-43
17	3,596	3,599	I	
19	3,591	3,593	I	
20	3,587	3,587	I	
21	3,579	3,581	I	
24	3,572	3,575	II	
⇒	3,571	3,573	III	Strong in Ud-114, Ud-29, Udf-43, F-43
26	3,567	3,568	II	
⇒	3,567	3,568	III	Strong in Ud-114, Ud-29, Udf-43, F-43
27⇒	3,556	3,556	IV	Strong in Ud-114, Ud-29, Udf-43, F-43
28	3,547	3,549	IV	
29	3,541	3,542	I	
⇒	3,541	3,542	III	Strong in Ud-114, Ud-29, Udf-43, F-43
32	3,525	3,529	I	
33	3,512	3,513	I	
38	3,480	3,483	I	
41	3,458	3,459	vw	
56	3,368	3,371	vw	
60	3,331	3,333	vw	

[a] Type I: a > > > c and b; Type II a > > c > b and a > c > b; Type III c > > a and b; Typ IV b > c > a

Synchrotron measurements

To check the homogeneity of the OH distribution, we analyzed some of the samples with synchrotron IR radiation with an aperture of 5 μm×5 μm and *E* polarized parallel to *a*. We choose two samples with high water content: one with OVMs (Ud-114) and another without (F-43). As expected, the intensities of the serpentine and talc (10 Å phase) bands vary by more than 50% from spot to spot in both samples. From TEM investigations, we know that the OVMs are caused by an

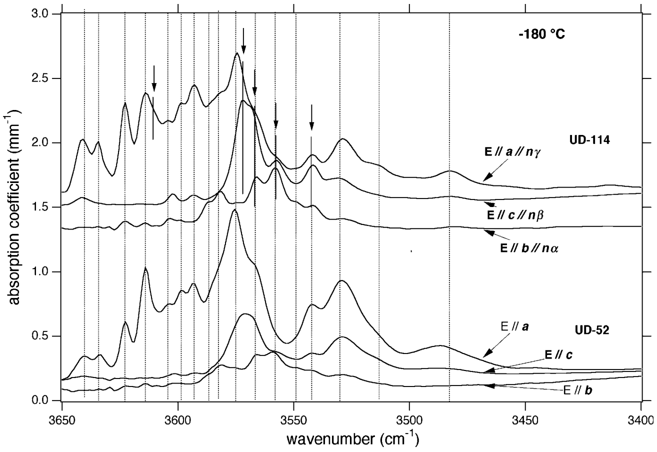

Fig. 4 Polarized infrared spectra of olivine samples UD-114 and UD-52 taken in situ at −180°C

array of submicron inclusions of serpentine, talc and 10 Å phase. The variability of A_{lin} for some other OH bands observed in the spectra of sample F-43 is shown in Fig. 5a–e. Figure 5f–j shows the variability of A_{lin} for the same OH bands but observed in the spectra of sample Ud-114. Sample F-43, the optical clear olivine, is very homogenous with respect to the OH distribution. The intensity ratios of the bands determined at different spots vary only slightly. However, in contrast to this sample, Ud-114 shows considerable variations of the OH band intensities from spot to spot. The largest spatial variation is observed for the bands at 3,624, 3,612, 3,591, 3,580 and 3,572 cm^{-1} ($E \parallel a$). The corresponding OH defects must be inhomogeneously distributed.

Annealing experiments

For Fe-bearing minerals, the reaction which is generally assumed to control dehydration involves oxidation of iron according to $\mathrm{Fe}^{2+} + \mathrm{OH}^{-} = \mathrm{Fe}^{3+} + \mathrm{O}^{2-} + 1/2\ \mathrm{H}_2$. And indeed, our results indicate that dehydration in olivine must also be associated with oxidation of Fe^{2+} as dehydration only occurs under heat treatment in air (Fig. 6). Figure 7 shows some selected IR spectra of Ud-170 after heat treatment in air at different temperatures. First, in the *a* polarized spectra, we observe that the OH bands which are related to serpentine (3,690 and 3,703 cm^{-1}) completely disappear at 550°C. The band at 3,677 cm^{-1} which is related to talc and 10 Å phase is, however, stable up to 900°C. In Fig. 8, A_{lin} of some OH bands is plotted as a function of temperature for all the dehydration experiments. The OH bands at 3,580, 3,591, 3,624, 3,630 and 3,638 cm^{-1} respond quite similar to the heat treatment, i.e., they start to diminish at 550°C and completely disappear at 950°C. The band around 3,612 cm^{-1} behaves in the same way, but the dehydration rate is more than two times faster as that for the other bands mentioned above indicating that this is a band system composed of two to three different OH bands (see above). The OH band(s) around 3,572 and 3,597 cm^{-1} behave different. The band(s) around 3,572 cm^{-1} slowly start to diminish at 750°C (Fig. 8a) in the spectra with $E \parallel a$. However, spectra taken with $E \parallel c$ reveal the complex character of the bands since here dehydration starts already at 650°C. This is an additional proof that the spectral range 3,570–3,572 cm^{-1} consists of type-II bands (polarized parallel to *a* and *c*) and type-III bands (strongly polarized parallel to *c*). The band at 3,597 cm^{-1} is stable up to about 900°C.

We observe three OH bands (3,672, 3,600 and 3,535 cm^{-1}) which keep constant in intensity with increasing temperature, but start to increase in intensity at about 850°C. All three bands are still present at 950°C where the other OH bands are disappeared (Figs. 7, 8b).

Starting at 650°C absorption increases in general in the spectral range 3,500–3,100 cm^{-1} and some weak bands appear. These bands are most likely due to liberated molecular water, which appears after the breakdown of the OH dipoles as clusters in the lamellar structure.

Secondary ion mass spectrometry

We observe no correlation between any of the trace elements measured and the water content (Table 3). The water content measured by SIMS was in all four samples lower than the water content calculated on the basis of the IR absorption calibration by Bell et al. (2003). As expected, the standard deviation for the olivine with the OVM is higher than for the OC crystals. Therefore, we used only the results of the OC crystals to calculate an integrated molar absorption coefficient for water in olivine. The value 37,500 ± 5,000 L mol $\mathrm{H_2O}$ cm^{-2} is within the uncertainties slightly higher than the value determined by Bell et al. (2003) (28,450 ± 1,830 L mol $\mathrm{H_2O}$ cm^{-2}). The IR absorption pattern of both sample sets (Bell et al. 2003 and this study) have minor contributions from inclusions of sheet silicates visible in the IR at high wavenumbers. As these inclusions also contribute to the water content determined by NRA and by SIMS absorption coefficient were in both studies calculated by integrating over the whole spectral range. A slightly higher value for the absorption coefficient for the olivine of this study is realistic since the absorption coefficients increase with the mean wavenumber of the corresponding OH bands (Libowitzky and Rossman 1997; Paterson 1982). Our spectra have a slightly different distribution of the absorption intensity than the spectra investigated by Bell et al. (2003). The IR calibration given by Libowitzky and Rossman (1997) for a mean wavenumber of 3,548 cm^{-1} as observed in our spectra yields an absorption coefficient of 50,553 L mol $\mathrm{H_2O}$ cm^{-2} and for a mean wavenumber of 3,570 cm^{-1} as observed in the spectra of Bell et al. (2003) a value of 45,128 L mol $\mathrm{H_2O}$ cm^{-2}, thus a comparable difference between our and Bell's et al. (2003) study. Olivine samples with a mean wavenumber of about 3,548 cm^{-1} should be quantified with the absorption coefficient as determined in this study.

Discussion and conclusion

Band assignment

Spectra of synthetic olivine are generally described to be composed of high-energy bands (group I bands: 3,450–3,650 cm^{-1}) and low-energy bands (group II bands: 3,100–3,450 cm^{-1}) (e.g., Bai and Kohlstedt 1993; Matveev et al. 2001; Lemaire et al. 2004). The interpretation of the nature of these bands is controversial. According to Bai and Kohlstedt (1993), hydrogen ions responsible for the high-energy bands are associated with metal vacancies in the octahedral positions while hydrogen

Fig. 5 Intensity correlations of OH bands within one sample (**a**–**e**) sample F-43 and (**f**–**j**) sample Ud-114

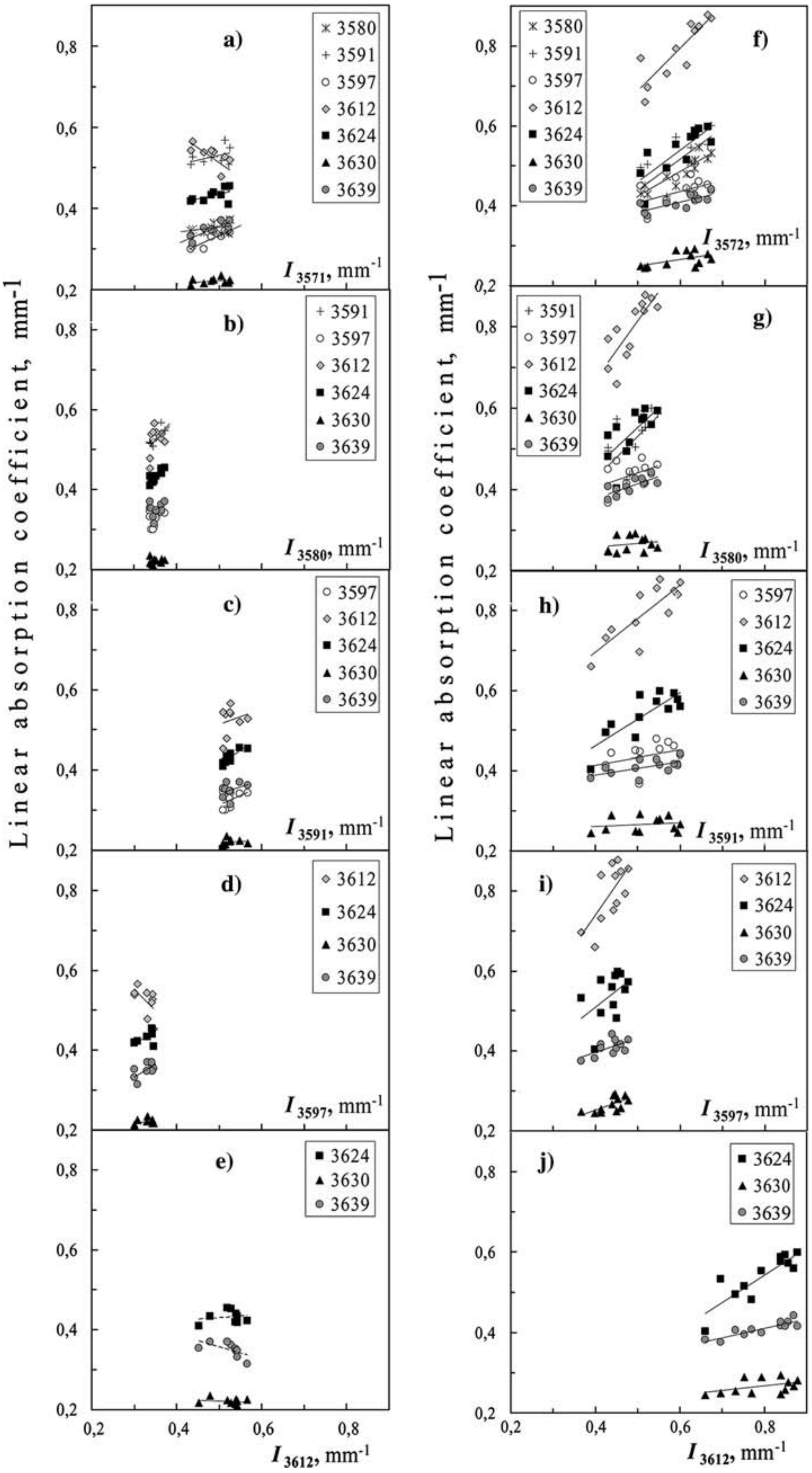

ions responsible for low-energy bands are associated with silicon tetrahedral vacancies. Later, Kohlstedt's group assigned all the OH bands in olivine exclusively to hydroxyls associated with metal vacancies (Kohlstedt et al. 1996; Kohlstedt and Mackwell 1998; Zhao et al. 2004). Matveev et al. (2001) synthesized olivine in

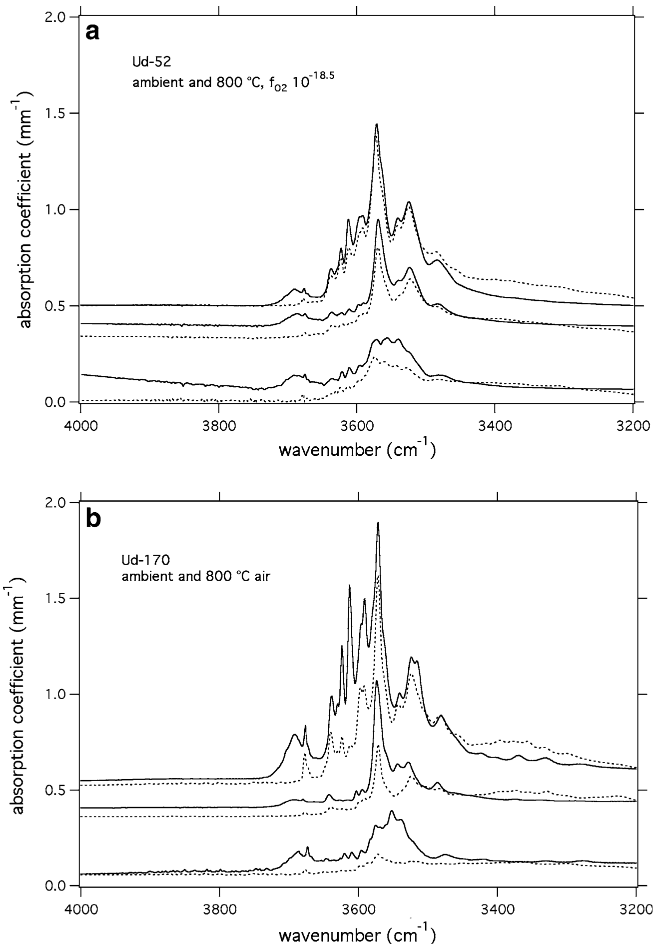

Fig. 6 Comparison of infrared spectra taken at room temperature before (*solid line*) and after (*dotted line*) annealing at 800°C (**a**) annealing under controlled low oxygen fugacity of $10^{-18.5}$ (**b**) annealing in air

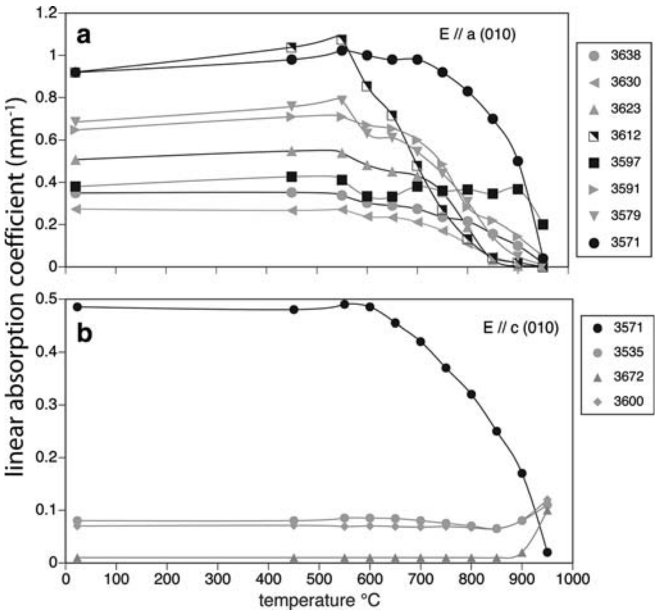

Fig. 8 Plot of the linear absorption coefficients versus temperature for some OH bands of sample Ud-170

equilibrium with magnesiowüstite and observed exclusive bands at high energy, which they interpreted to be associated with vacant silicon sites, while olivine synthesized in equilibrium with orthopyroxene shows group II bands, thus associated with hydroxyl in octahedral sites. Lemaire et al. (2004) investigated the effect of silica activity on the incorporation of water in forsterite and generally confirmed the results of Matveev et al. (2001). At low silica activity, Lemaire et al. (2004) observed group I bands (3,613, 3,580, 3,566, 3,555 and 3,480 cm^{-1}), thus associated with protonated silicon vacancies; however, these bands remain even at high

Fig. 7 Infrared spectra of stepwise annealed olivine sample Ud-170 (RT-950°C) after quenching. At each step, the spectra were taken at the same spot. At 950°C an additional spectrum was taken at the rim [950°C(R)]

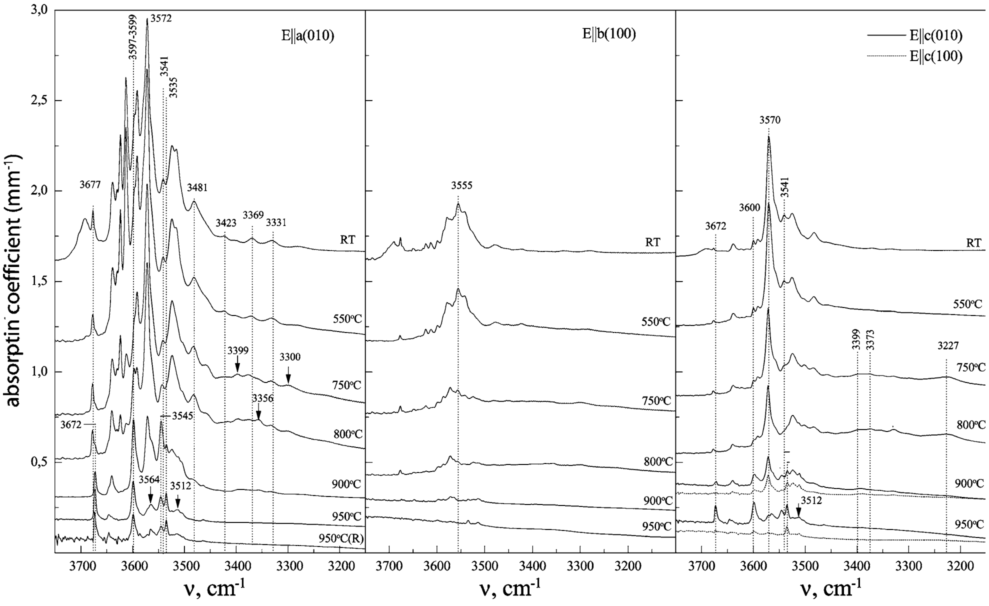

Table 3 Trace element compositions in ppm by wt and the water content for olivine xenocrysts from Udachnaya (1σ standard deviation)

Sample no.	T(°C) de Hoog (2004)	B	Li	Al	Cr	Mn	Ca	H_2O	
								ppm by wt SIMS	ppm by wt IR, Bell et al. (2003)
Ud-29	1,041	0.14 (0.16)	0.96 (0.09)	24.90 (2.1)	380 (6)	600 (12)	97 (7)	162 (16)	195
F-43	1,012	0.04 (0.01)	1.2 (0.1)	20.4 (0.5)	224 (6)	680 (16)	92 (3)	234 (39)	297
Ud-170	1,058	0.16 (0.05)	1.0 (0.1)	27.7 (0.8)	273 (12)	715 (20)	120 (8)	272 (107)	300
Ud-52	1,122	0.30 (0.03)	2.2 (0.3)	41 (1)	202 (15)	1,029 (71)	162 (13)	205 (23)	287
Synthetic olivine		0.03 (0.02)	0.02 (0.01)	2.8 (0.5)	85 (11)	1.5 (0.2)	56 (21)	8 (2)	8

[a] Calculated using geothermometer by de Hoog (2004)

silica activity. The bands observed at higher silica activity (3,160, 3,220 and 3,600 cm^{-1}) are assigned to OH groups associated with M-site vacancies.

The atomic environment around a vacant Si tetrahedron as proposed by Lemaire et al. (2004) is shown in Fig. 9. They assigned the band at 3,612 cm^{-1} which is strongly polarized with $E \parallel a$ to vibrations of an O(1)–H dipole pointing exactly to the vacant silicon site. This is our type-I polarization. The OH band at 3,580 cm^{-1} shows maximum absorption with $E \parallel a$ and a smaller contribution with $E \parallel b$, c (our type-II polarization). Lemaire et al. (2004) assign this band to hydrogen located along the O2–O1 join of a vacant tetrahedron. Another band at 3,567 cm^{-1}, which is strongly polarized parallel to c is assigned to H located along the O3–O3 edge of the tetrahedron and thus oriented along c (our type-III). The bands at 3,555 cm^{-1} ($E \parallel b$ with contribution to a and c) and 3,480 ($E \parallel a$ and $E \parallel b$) cm^{-1} are much weaker than the bands described above and Lemaire et al. (2004) did not interprete them. From the pleochroic scheme, it is identical with our type-IV polarization. As shown before, we observe OH bands with similar band positions and pleochroic behavior. These bands were most pronounced in the samples Ud-114, F-43, Ud-29 and Udf-43. The bands correlate with intensity (band correlation group I). Therefore, we assign these OH bands to OH associated with vacant Si tetrahedra. In detail, these are all the bands of the type-III and type IV polarization and some are of the type-I polarization (3,612 and 3,597 cm^{-1}). We assigned the 3,597 cm^{-1} band to be related to vacant Si tetrahedra because it responds in the same way as the bands at 3,567–3,571 cm^{-1} to the heat treatment, i.e., both bands were very stable during heat treatment and did not decrease in intensity as fast as the most of the other bands. In a theoretical study, Braithwaite et al. (2003) applied computer modeling techniques to study the structure and energetics of H defects in forsterite. According to them, there is a strong driving force for hydroxyl groups to combine with cation vacancies so that charge compensation can take place. They propose that H defects in forsterite will be associated with both Si and Mg vacancies. According to them, the most likely defect associated with a silicon vacancy is $(3H)'_{Si}$, i.e., a silicon vacancy associated with the incorporation of three hydrogen atoms. For charge compensation, such a defect must be stabilized by some other impurities, such as a neighboring M^{3+} cation at an M^{2+} site. The proposed sites and OH directions are very similar to the results of Lemaire et al. (2004) and to our results. However, we cannot decide from the spectra whether the fully protonated Si defect or the $(3H)_{Si}$ defect is present in our samples. In the annealing experiments, we observed OH bands, which increase with increasing temperature in intensity. An interesting hypothesis would be that these bands are associated with Fe^{3+} and thus increase with increasing oxidation of the samples.

Altogether, however, with this assignment only 20–30% of the observed OH bands in our study can be explained. There must be an additional defect mechanism with OH dipoles exclusively aligned parallel to a. Libowitzky and Beran (1995) pointed out that a common significant feature of natural olivine OH spectra is the strong polarization of the most of the high frequency bands with E parallel to a. They observed sharp strongly pleochroic band doublets with similar distances and pleochroic behavior centers at 3,674/3,624, 3,647/3,598 and 3,640/3,592. They suggest that these bands are due to OH stretching vibrations of O1–H dipoles pointing directly to the vacant Si site (parallel to a). Another OH doublet (3,570/3,535) shows a strong absorption parallel to a and c. This doublet is explained by Libowitzky and Beran (1995) by OH groups oriented along the O3–O1 tetrahedral edge and OH groups oriented along the O2–O3 edge of a vacant M site. The splitting of the bands is explained by different chemical environments (Mg substituted by Fe^{2+}). However, again this assignment may be correct for the sample studied by Libowitzky and Beran (1995) and is very similar to the proposals of the above-mentioned recent studies but it cannot explain all of the observed OH bands in our study. For one Si vacancy, we need for charge compensating four hydrogens [or three in the case of a $(3H_{Si})'$ defect] which would give rise to four (three) OH bands. But according to the proposed hydrogen incorporation mechanism just one of these OH bands would be strongly polarized parallel to a, namely the O1–H dipole band. To explain the additional OH bands, an additional defect must be introduced.

Experiments and observations in nature show that the solubility of hydrogen in endmember and near endmember forsterite is very limited (Libowitzky and

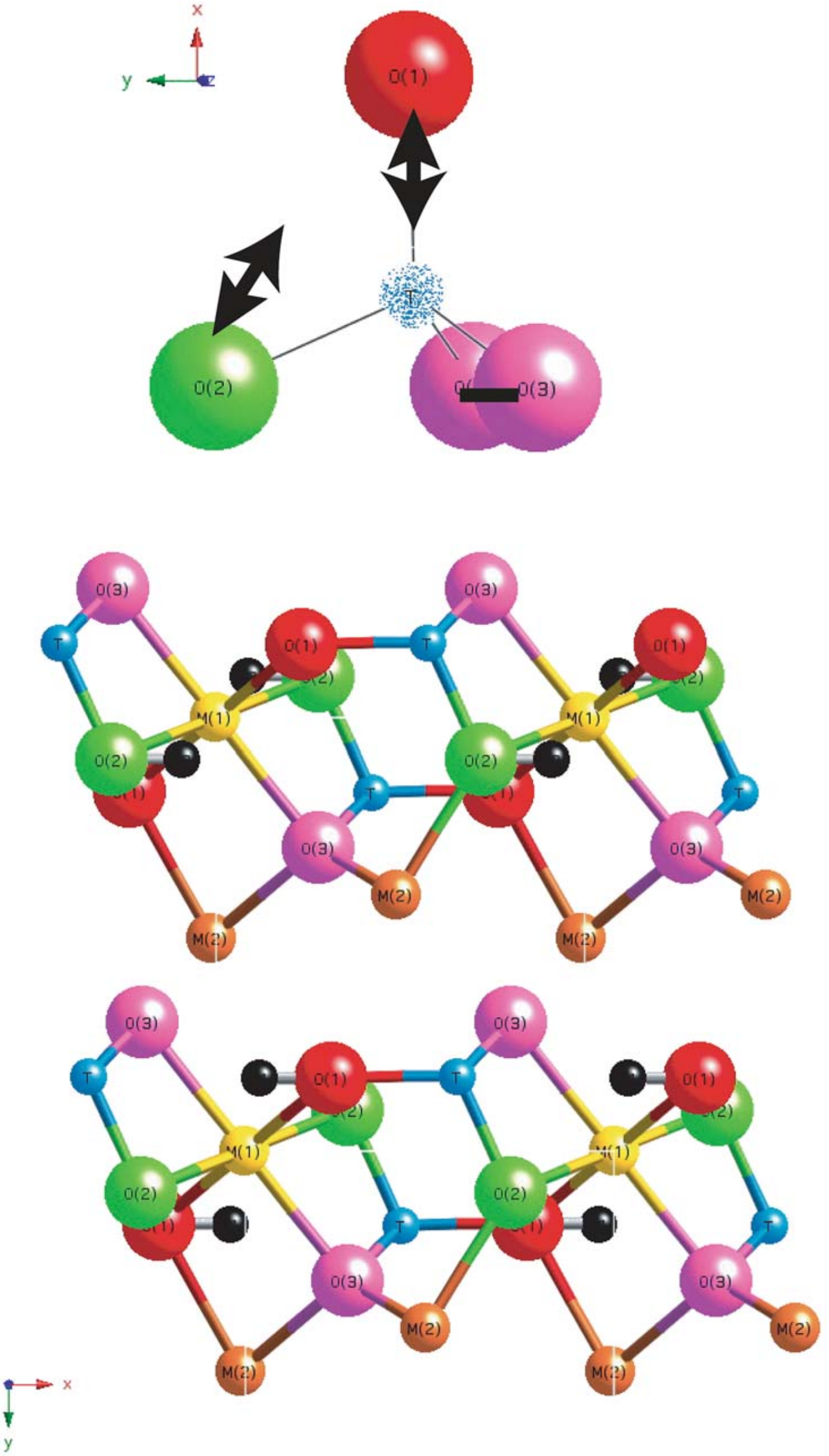

Fig. 9 *Upper part*: plot of the atomic environment around a vacant Si site after Lemaire et al. (2004). The *arrows* represent directions of the OH vectors. The *bold line* represent an OH vector which is strongly aligned parallel *c* along the O3–O3 direction. *Lower parts*: part of the olivine structure showing the proposed hydrogens (*black balls*) associated with vacant M1 sites and either bonded to O(2) or to O(1)

Beran 1995; Demouchy and Mackwell 2003; Zhao et al. 2004), while the hydrogen solubility increases with increasing Fe content. According to Zhao et al. (2004) and based on the point defect model derived by Nakamura and Schmalzried (1983), this is due to an increase of metal vacancy concentration with increasing

Fe content. Thus, it is generally believed that the major point defect associated with hydrogen incorporation in Fe-bearing olivine can be described as $(2H)^x_{Mg}$. This would explain why Libowitzky and Beran (1995) observed in their forsterite spectra a much smaller number of OH bands as we in our more Fe-rich olivine spectra. Thus, it is very likely that mantle olivine shows a significant number of M vacancies.

Matveev et al. (2005), Lemaire et al. (2004) and Braithwaite et al. (2003) propose that the low energy bands in olivine which occur around 3,100–3,250 cm^{-1} and which are polarized with $E \parallel c$, must be assigned to OH groups associated with M-site vacancies. In our natural mantle olivine spectra we neither observe OH bands at such low energies nor we observe intense band with such a polarization behavior. But it is very unlikely that we do not have metal vacancies.

On the basis of the observed pleochroic scheme (bands very intense with $E \parallel a$), we propose that the most of our Type-I OH bands are associated with vacant M1 sites charge balanced by two hydrogens whose OH dipole directions are both strongly aligned parallel to *a* (Fig. 9). We introduce two different methods for hydrogen incorporation in olivine which may be realized simultaneously. In some vacant M1 sites, H1 is bonded to O1 exhibiting bifurgated hydrogen bonding to the O3 and O2 oxygens. Here, the Si–O1–H1 atoms build a line and the OH dipole points directly away from the Si site (parallel to *a*). In other vacant M1 sites, H2 is bonded to O2 exhibiting bifurgated hydrogen bonding to O1 and O3. Here, the O2–H2 dipole is also strongly aligned parallel to *a* (Fig. 9). Charge balancing at a vacant M^{2+} site needs two H^+. As the M1 site has a center of symmetry, an OH dipole associated with M1 occurs in both cases as pairs and gives rise to a single type of OH band. In both configurations, O1–H1 and O2–H2, the angle of the corresponding O–H ···O bond is with 130–136° in a realistic range, e.g., as observed for bifurgated O–H ···O bonds in staurolite. We expect repulsion of neither the H1–H1 nor H2–H2 atoms, as the corresponding distances between the hydrogens are too large (3.36 and 3.30 Å, respectively). The O1–H1 groups may be responsible for OH bands occurring at lower wavenumbers (mean O–O distance in the bifurgated bond 2.85 Å) compared to the OH bands assigned to O2–H2 (mean O–O distance in the bifurgated bond 3.10 Å). Type-II bands are also assigned to this type of defect; they only deviate to a small degree from the strong *a* polarization of the type-I bands. The fact that more than two bands, one due to O1–H1 and another due to O2–H2 exist can be explained by different chemical environments of the hydroxyl groups and/or by slightly different distortions of the M1 sites in these high-pressure olivines. It is generally believed that olivine at upper-mantle conditions deforms essentially by dislocation creep with a predominant [100] slip (Mainprice et al. 2005). Such deformation could be responsible for slightly different O–O distances for one and the same defect type and thus results in slightly different band positions.

Development and origin of the observed microstructure

As mentioned above, we investigated two series of mantle olivine: some with OVMs and some with OC. We found two very interesting differences between these two series.

Synchrotron measurements revealed that in the OC samples, the OH defects are homogenously distributed in contrast to the other samples (OVM). In the OVM samples, the intrinsic but also the extrinsic defects are very inhomogeneously distributed.

In the samples F-64, Ud-85 and Udf-43, the serpentine and talc inclusions are oriented with respect to the host olivine. The corresponding OH bands show the highest intensity with $E \parallel a$ of the olivine lattice. Interestingly, these samples have the highest concentration of serpentine and talc as compared to the other six samples (17–27% of the integral absorbances vs. 3–6%) and they have the lowest water content of all samples under study. We interprete these observations such that the different olivine types represent different stages of P, T regime of the olivine during ascent of the sample to the surface as a function of time:

Stage 1: represented by clear water-rich olivine without any inclusions. These are water saturated olivines grown at high pressure.

Stage 2: approaching lower pressure the solubility of water in olivine decreases and the formerly incorporated OH defects begin to migrate and concentrate as OH-bearing inclusions, such as “hydrous olivine”, 10 Å phase, talc and finally serpentine. This stage is represented by the strong inhomogenous distribution of the intrinsic OH bands in sample Ud-114, for example, and the visible microstructures.

Stage 3: the water concentration in olivine of stage 3 is very low and the concentration of inclusions relatively high. The inclusions are oriented with respect to the olivine lattice (F-64, Ud- 85 and Udf-43).

Acknowledgements We thank U. Schade who helped with the synchrotron measurements at Bessy II, Berlin, Germany, R. Schulz for conducting the experiments in the rapid-quench gas flow furnace and M. Wiedenbeck for helpful discussions and suggestions concerning the SIMS measurements. The comments and suggestions of A. Beran and an anonymous reviewer helped to clarify and improve the manuscript. The grants 436 UKR 17/15/03 and -/04 for S.S. Matsyuk and 436 RUS 17/75/03 and -/76/04 for N. Khisina by Deutsche Forschungsgemeinschaft DFG are gratefully acknowledged.

References

Bai Q, Kohlstedt DL (1993) Effects of chemical environment on the solubility and incorporation mechanism for hydrogen in olivine. Phys Chem Miner 19:460–471

Bell DR, Rossman GR, Maldener J, Endisch D, Rauch F (2003) Hydroxide in olivine: a quantitative determination of the absolute amount and calibration of the IR spectrum. J. Geophys Res 108(B2):2105–2113

Beran A (1969) Über OH-Gruppen in Olivin. Österr Akad Wiss, Math Naturw Kl Anzeiger:73–74

Beran A, Putnis A (1983) A model of the OH positions in olivine, derived from infrared-spectroscopic investigations. Phys Chem Miner 9:57–60

Braithwaite JS, Sushko PV, Wright K, Catlow CRA (2002) Hydrogen defects in forsterite: a test case for the embedded cluster method. J Chem Phys 116:2628–2635

Braithwaite JS, Wright K, Catlow CRA (2003) A theoretical study of the energetics and IR frequencies of hydroxyl defects in forsterite. J Geophys Res 108(B6):2284

De Hoog JC (2004) An empirical calibration of an Al-in-olivine geothermometer for mantle-derived materials. EOS Trans Am Geophys Union Suppl 85:V41C-1399

Demouchy S, Mackwell S (2003) Water diffusion in synthetic iron-free forsterite. Phys Chem Miner 30:486–494

Khisina NR, Wirth R, Andrut M, Ukhanov AV (2001) Extrinsic and intrinsic mode of hydrogen occurrence in natural olivines: FTIR and TEM investigation. Phys Chem Miner 28:291–301

Kitamura M, Kondoh S, Morimoto N, Miller GH, Rossman GR (1987) Planar OH-bearing defects in mantle olivine. Nature 328:143–145

Kohlstedt DL, Mackwell SJ (1998) Diffusion of hydrogen and intrinsic point defects in olivine. Z Phys Chem 207:147–162

Kohlstedt DL, Keppler H, Rubie DC (1996) Solubility of water in the α, β, and γ phases of $(Mg, Fe)_2SiO_4$. Contrib Mineral Petrol 123:345–357

Kurosawa M, Yurimoto H, Sueno S (1997) Patterns in the hydrogen and trace element compositions of mantle olivines. Phys Chem Miner 24:385–395

Lemaire C, Kohn SC, Brooker RA (2004) The effect of silica activity on the incorporation mechanisms of water in synthetic forsterite: a polarised infrared spectroscopic study. Contrib Mineral Petrol 147:48–57

Libowitzky E, Beran A (1995) OH defects in forsterite. Phys Chem Miner 22:387–392

Libowitzky E, Rossman GR (1997) An IR absorption calibration for water in minerals. Am Mineral 82:1111–1115

Mainprice D, Tommasi A, Couvy H, Cordier P, Frost DJ (2005) Pressure sensitivity of olivine slip systems and seismic anisotropy of Earth's upper mantle. Nature 233:731–733

Maldener J, Hösch A, Langer K, Rauch F (2003) Hydrogen in some natural garnets studied by nuclear reaction analysis and vibrational spectroscopy. Phys Chem Miner 30:337–344

Matsyuk SS, Langer K (2004) Hydroxyl in olivines from mantle xenoliths in kimberlites of the Siberian platform. Contrib Mineral Petrol 147:413–437

Matveev S, O'Neill HSC, Ballhaus C, Taylor WR, Green DH (2001) Effect of silica activity on OH-IR spectra of olivine: implications for low-a_{SiO2} mantle metasomatism. J Petrol 42:721–729

Matveev S, Portnyagin M, Ballhaus C, Brooker R, Geiger CA (2005) FTIR spectrum of phenocryst olivine as an indicator of silica saturation in magmas. J Petrol 46:603–614

Miller GH, Rossman GR, Harlow GE (1987) The natural occurrence of hydroxide in olivine. Phys Chem Miner 14:461–472

Nakamura A, Schmalzried H (1983) On the nonstoichiometry and point defects of olivine. Phys Chem Miner 10:27–37

Paterson (1982) The determination of hydroxyl by infrared absorption in quartz, silicate glasses and similar materials. Bull Minéral 105:20–29

Sykes D, Rossman GR, Veblen DR, Grew ES (1994) Enhanced H and F incorporation in borian olivine. Am Mineral 79:904–908

Wiedenbeck M, Rhede D, Lieckefett R, Witzki H (2004) Cryogenic SIMS and its applications in the earth sciences. Appl Surf Sci 231–232:888–892

Zhao YH, Ginsberg SB, Kohlstedt DL (2004) Solubility of hydrogen in olivine: dependence on temperature and iron content. Contrib Mineral Petrol 147:155–161